RESEARCH ARTICLE

OCEAN NUTRIENTS

Natural iron fertilization by shallow hydrothermal sources fuels diazotroph blooms in the ocean

Sophie Bonnet[1]*, Cécile Guieu[2]*, Vincent Taillandier[2], Cédric Boulart[3], Pascale Bouruet-Aubertot[4], Frédéric Gazeau[2], Carla Scalabrin[5], Matthieu Bressac[2], Angela N. Knapp[6], Yannis Cuypers[4], David González-Santana[7,8], Heather J. Forrer[6], Jean-Michel Grisoni[9], Olivier Grosso[1], Jérémie Habasque[7], Mercedes Jardin-Camps[1], Nathalie Leblond[9], Frédéric A. C. Le Moigne[1,7], Anne Lebourges-Dhaussy[7], Caroline Lory[1], Sandra Nunige[1], Elvira Pulido-Villena[1], Andrea L. Rizzo[10,11], Géraldine Sarthou[7], Chloé Tilliette[2]

Iron is an essential nutrient that regulates productivity in ~30% of the ocean. Compared with deep (>2000 meter) hydrothermal activity at mid-ocean ridges that provide iron to the ocean's interior, shallow (<500 meter) hydrothermal fluids are likely to influence the surface's ecosystem. However, their effect is unknown. In this work, we show that fluids emitted along the Tonga volcanic arc (South Pacific) have a substantial impact on iron concentrations in the photic layer through vertical diffusion. This enrichment stimulates biological activity, resulting in an extensive patch of chlorophyll (360,000 square kilometers). Diazotroph activity is two to eight times higher and carbon export fluxes are two to three times higher in iron-enriched waters than in adjacent unfertilized waters. Such findings reveal a previously undescribed mechanism of natural iron fertilization in the ocean that fuels regional hotspot sinks for atmospheric CO_2.

Planktonic diazotrophs are microscopic organisms ubiquitous in the ocean that play a crucial role: They supply available nitrogen (N), an essential but scarce nutrient in most of the oceans, to the surface ocean biosphere (*1*, *2*). Diazotrophs do so by converting atmospheric N_2 (endlessly available but metabolically useless) to ammonia (readily bioavailable), a reaction termed biological N_2 fixation. Diazotrophs thus alleviate N limitation in 60% of the oceans, especially in low latitudes. This promotes CO_2 fixation by phytoplankton into organic carbon (primary productivity) that, in turn, sustains the food web and organic carbon export and sequestration to the deep ocean (*3*–*6*). However, diazotrophs face a major challenge: Besides phosphorus requirements, the iron (Fe)–rich nitrogenase enzyme that catalyzes N_2 fixation imposes a high Fe demand on diazotroph growth (*7*), but Fe bioavailability in the ocean often limits the growth of these organisms (*6*, *8*). The western tropical South Pacific (WTSP) Ocean is a recognized hotspot of N_2 fixation activity, with an estimated contribution of ~21% to the global fixed N input (*9*). Fe supply through atmospheric deposition is known to control large-scale diazotroph biogeography (*10*), but such aeolian inputs are extremely low in this remote region (*11*), which suggests that alternative Fe fertilization processes underlie the ecological success of diazotrophs. Identifying these processes is of the utmost importance because diazotrophs have recently been identified as key drivers of future marine net primary productivity in response to climate change (*12*). In this work, we demonstrate that Fe-rich fluids emitted by shallow hydrothermal venting directly fertilize the overlying surface ecosystem, which induces intense diazotroph activity that supports enhanced carbon export fluxes, with a C sequestration efficiency higher than those from artificial mesoscale Fe-addition experiments.

The WTSP hosts the Tonga-Kermadec subduction zone, which stretches 2500 km from New Zealand to Tonga (Fig. 1A). It is the fastest-converging, most seismically active subduction zone and has the highest density of underwater volcanic centers on Earth (*13*). This system produces extensive plumes of ^{3}He in the bathypelagic ocean (1500 to 2000 m) that fingerprint deep hydrothermal sources originating in the Lau Basin (*14*, *15*). Other authors (*16*, *17*) identified shallower sources (<500 m) along the Tonga arc, which are associated with elevated dissolved Fe (DFe) and manganese (DMn) concentrations close to the seafloor. Guieu *et al.* (*11*) demonstrated that these shallow sources were able to bring DFe up to the photic layer (~100 m) at high concentrations (up to 66 nmol liter^{-1}). These Fe infusions are hypothesized to fuel the observed N_2 fixation hotspot associated with a patch of increased chlorophyll that persists 6 months per year in this region (Fig. 2, A and B) (*9*, *11*). Yet, there is, at present, no empirical evidence of the direct effect of such hydrothermal Fe fertilization on the overlying planktonic ecosystem, with the implication that a substantial part of N entering the subtropical Pacific, owing to hydrothermal Fe, is likely missing from N budgets. Such an Fe supply mechanism would challenge the prevailing paradigm that diazotroph productivity is mainly mediated by Fe from dust deposition (*10*) in N-limited regions.

To document the mechanistic link between Fe supply from submarine volcanism and the response of the surface plankton community, we combined acoustic, chemical, physical, and biological data acquired during the GEOTRACES GPpr14 TONGA expedition (*18*), a zonal transect between the Tonga volcanic arc and the South Pacific Gyre, which serves as a reference deep-sea site where the ocean surface is not affected by hydrothermal activity. The targeted submarine volcano [volcano 1 (*16*, *17*)] is a large stratovolcano (basal diameter 28 km) located in the central part of the Tonga arc (21°09.24′S; 175°44.64′W) (Fig. 1, A and B). During an acoustic survey above the volcano, we detected multiple acoustic plumes (Fig. 1B and table S1) rising from the sea floor up to ~20 m below the ocean surface (Fig. 1C). We focused our study on a site located near the caldera on the southwestern edge of the volcano (Fig. 1B) (hereafter referred to as the "Panamax site"), where the acoustic anomaly (*19*–*21*), which is also associated with intense gas-bubble emissions, was strong and continuous (Fig. 1D). Repeated conductivity, temperature, and depth (CTD) casts at this site revealed that acoustic plumes were also associated with strong anomalies in pH, turbidity, and redox potential (Eh) (Fig. 1E and table S2) from the seafloor (195 m depth) up to ~160 m. Methane concentrations that reached >100 nmol liter^{-1} (Fig. 1F) and the excess of ^{3}He and ^{4}He concentrations (fig. S1 and table S3) confirmed the hydrothermal origin of the plumes.

DFe and DMn were also enriched ~80-fold at this site (Fig. 1F) compared with similar depths in the WTSP (*11*, *22*). DFe and methane (CH_4) concentrations were positively correlated [coefficient of determination (R^2) = 0.89, $p < 0.05$]. DFe reached concentrations as high

[1]Aix Marseille University, Université de Toulon, CNRS, IRD, MIO Marseille, France. [2]Laboratoire d'Océanographie de Villefranche (LOV), Institut de la Mer de Villefranche, CNRS, Sorbonne Université, 06230 Villefranche-sur-Mer, France. [3]Adaptation et Diversité en Milieu Marin, UMR 7144 AD2M CNRS-Sorbonne Université, Station Biologique de Roscoff, 29680 Roscoff, France. [4]Laboratoire d'Océanographie et du Climat: Expérimentation et Approches Numériques (LOCEAN-IPSL), Sorbonne University, CNRS-IRD-MNHN, 75005 Paris, France. [5]Ifremer, Univ Brest, CNRS, UMR 6538 Geo-Ocean, F-29280 Plouzané, France. [6]Department of Earth, Ocean, and Atmospheric Sciences, Florida State University, Tallahassee, FL 32306, USA. [7]CNRS, Univ Brest, IRD, Ifremer, UMR 6539, LEMAR, Plouzané, France. [8]Instituto de Oceanografía y Cambio Global (IOCAG), Universidad de Las Palmas de Gran Canaria, 35017 Las Palmas, Spain. [9]Institut de la Mer de Villefranche, IMEV, Sorbonne Université, Villefranche-sur-Mer, France. [10]Istituto Nazionale di Geofisica e Vulcanologia, Sezione di Milano, Via Alfonso Corti 12, 20133 Milano, Italy. [11]Department of Earth and Environmental Sciences, University of Milano-Bicocca, Piazza della Scienza 4, 20126 Milan, Italy.
*Corresponding author. Email: sophie.bonnet@mio.osupytheas.fr (S.B.); cecile.guieu@imev-mer.fr (C.G.)

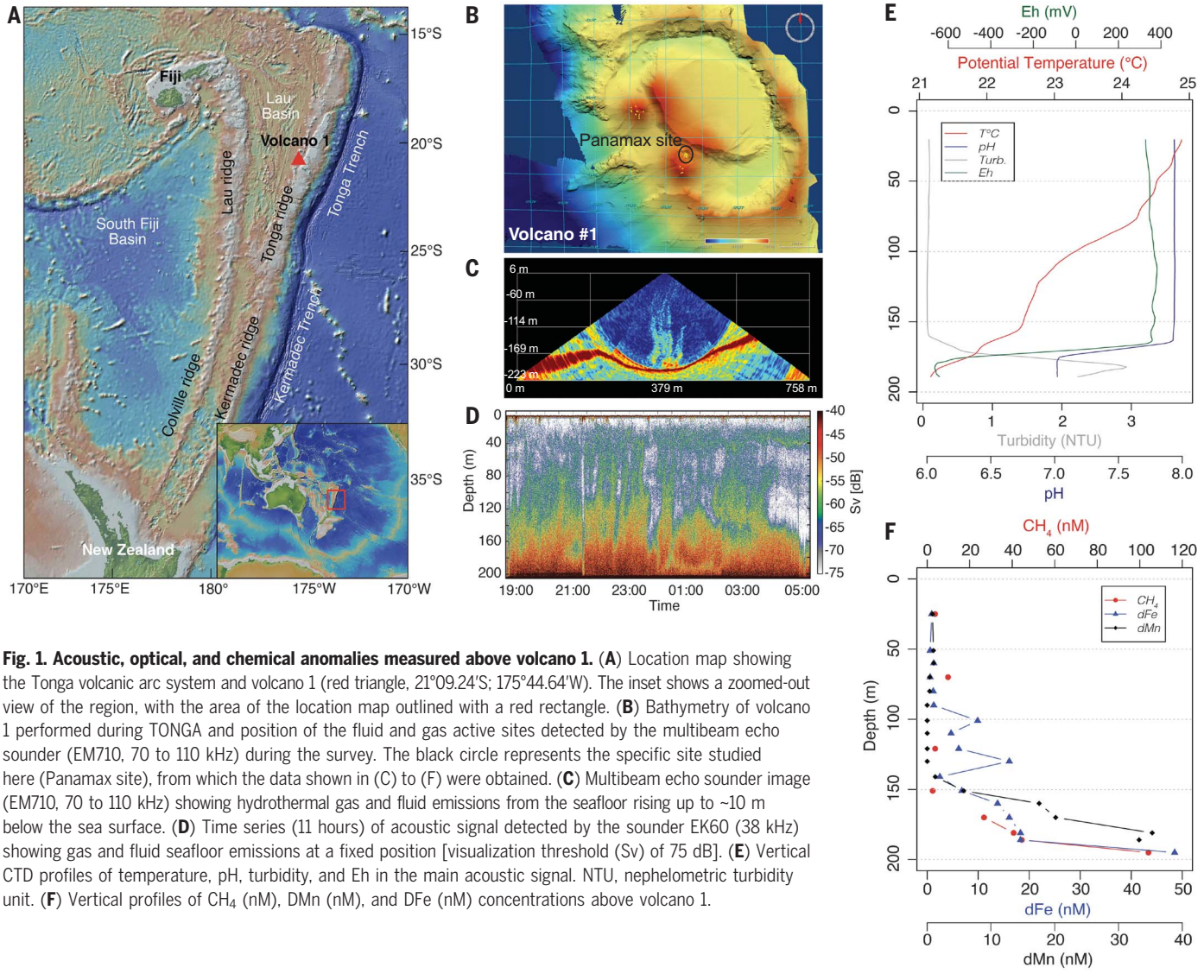

Fig. 1. Acoustic, optical, and chemical anomalies measured above volcano 1. (**A**) Location map showing the Tonga volcanic arc system and volcano 1 (red triangle, 21°09.24′S; 175°44.64′W). The inset shows a zoomed-out view of the region, with the area of the location map outlined with a red rectangle. (**B**) Bathymetry of volcano 1 performed during TONGA and position of the fluid and gas active sites detected by the multibeam echo sounder (EM710, 70 to 110 kHz) during the survey. The black circle represents the specific site studied here (Panamax site), from which the data shown in (C) to (F) were obtained. (**C**) Multibeam echo sounder image (EM710, 70 to 110 kHz) showing hydrothermal gas and fluid emissions from the seafloor rising up to ~10 m below the sea surface. (**D**) Time series (11 hours) of acoustic signal detected by the sounder EK60 (38 kHz) showing gas and fluid seafloor emissions at a fixed position [visualization threshold (Sv) of 75 dB]. (**E**) Vertical CTD profiles of temperature, pH, turbidity, and Eh in the main acoustic signal. NTU, nephelometric turbidity unit. (**F**) Vertical profiles of CH_4 (nM), DMn (nM), and DFe (nM) concentrations above volcano 1.

as 48.5 nmol liter^{-1} at 195 m (within the main acoustic signal), and although they decreased toward the photic layer (~0 to 100 m), DFe concentrations in that layer (~0.6 to 10 nmol liter^{-1}) (Fig. 1F) were one order of magnitude higher compared with those at stations not affected by hydrothermal activity (*23*). The turbulence profiles (fig. S2) revealed an order of magnitude higher vertical diffusivity above the volcano ($K_z = 3.7 \pm 1.9 \times 10^{-5}$ m^2 s^{-1} at ~50 m, which corresponds to the base of the surface mixed layer) compared with the distal open-sea reference site ($K_z = 5.2 \pm 9.6 \times 10^{-6}$ m^2 s^{-1}) (Table 1), in line with previous work above shallow (~200 m) seamounts (*24*). Combining the measured K_z with the DFe gradients (Table 1 and supplementary materials), the diffusive DFe vertical supply to the mixed layer above the volcano reached $1.1 \pm 1.7 \times 10^{-4}$ mmol Fe m^{-2} day^{-1}. This is orders of magnitude larger than the value at the reference site (Table 1), which suggests that Fe-rich fluids released close to the shallow volcano represent a major Fe source to surface waters. A phosphate supply of $5.4 \pm 2.4 \times 10^{-3}$ mmol m^{-2} day^{-1} accompanied this vertical DFe supply, whereas no nitrate supply could be quantified (table S5) because of the decoupling between the depth of the phosphacline (~50 m) and the nitracline (~100 m) (fig. S5), as already observed in the WTSP (*25*).

Along the west-to-east zonal transect, total chlorophyll a (Chla) and particulate organic N stocks peaked in the naturally Fe-fertilized waters at volcano 1 (Fig. 2). Both were also elevated up and downstream of the arc (Fig. 2, C and D), consistent with ocean color images (Fig. 2A). This biomass peak was associated with N_2 fixation rates enhanced two- to eightfold relative to surrounding waters on either side of the arc ($p < 0.05$, Mann-Whitney test) (Fig. 2E) and 90-fold higher *Trichodesmium* spp. abundances ($p < 0.05$, Mann-Whitney test) (Fig. 2F). This led to extremely high N_2 fixation rates and *Trichodesmium* spp. abundances in the Fe-fertilized waters (>2000 μmol N m^{-2} day^{-1}; ~6×10^7 *nifH* gene copies liter^{-1}, where *nifH* is the gene that encodes a subunit of the nitrogenase enzyme that catalyzes N_2 fixation), that is, values one to two orders of magnitude greater than those commonly found in other (sub)tropical ocean basins (*26*). This peak in diazotroph activity was marked by a phosphate drawdown (~50 nM) in the photic layer, although concentrations were not limiting for *Trichodesmium* spp. (*27*) because of intense microbial phosphorus cycling in this region (*28*). Diazotrophs were favored by the extremely low nitrate concentrations along the transect (fig. S6).

The particulate organic carbon (POC) and nitrogen (PON) export fluxes were measured using surface tethered sediment traps deployed for 4 days near volcano 1 and at the reference site. Consistent with model simulations in this region (*22*), POC export at 170

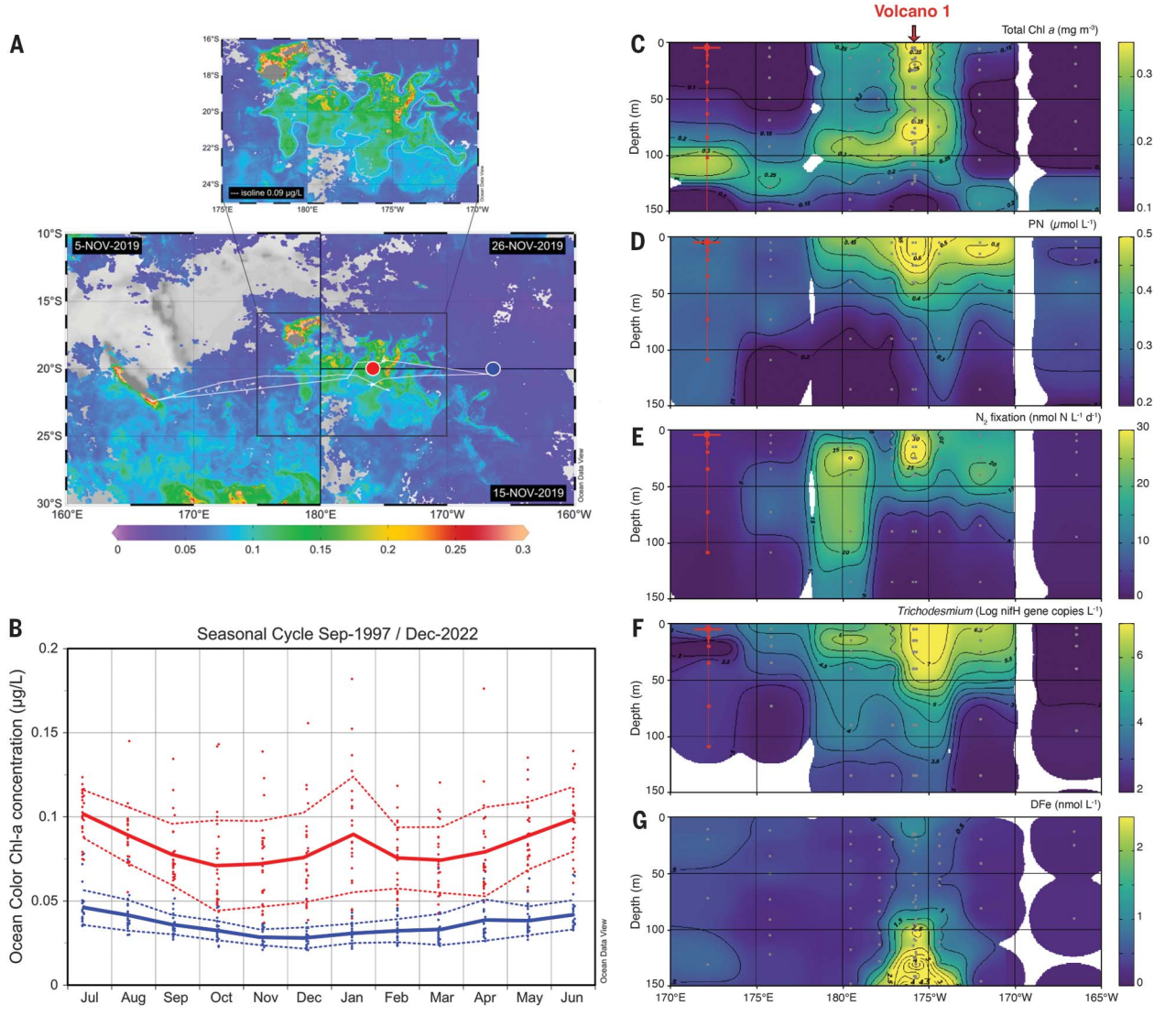

Fig. 2. Chlorophyll patch in the vicinity of Tonga and associated biogeochemical and biological parameters. (**A**) Surface [Chla] [GlobColour chlorophyll-a product based on multisensor satellite observations (SeaWiFS, MERIS, MODIS, VIIRS, and OLCI)] averaged over the time period corresponding to the TONGA cruise (1 November to 6 December 2019) at a resolution of 4 km and zoom-in of the bloom region (~360,000 km^2). The bloom is delineated by the isoline 0.9 µg liter^{-1} (which corresponds to twice the average background [Chla] outside the bloom). The red and blue circles represent the reference sites for the data shown in (B). (**B**) Monthly climatology of [Chla] from a 25-year time series [GlobColour chlorophyll-a product based on multisensor satellite observations (SeaWiFS, MERIS, MODIS, VIIRS, and OLCI)] at two sites along 20°S; the solid red line represents the multiyear average at monthly resolution in the region of the Tonga bloom represented with the red circle in (A), and the solid blue line corresponds to the location of the reference site in the South Pacific Gyre, represented as a blue circle in (A). The red and blue dashed lines represent the standard deviation. (**C** to **G**) Horizontal and vertical distributions of (C) total Chla concentrations (µg liter^{-1}), (D) particulate organic nitrogen (PN) concentrations (µmol liter^{-1}), (E) N_2 fixation rates (nmol N liter^{-1} day^{-1}), (F) *Trichodesmium* abundances (log *nifH* gene copies liter^{-1}), and (G) DFe concentrations (nmol liter^{-1}). The *y* axis shows depth (m), and the *x* axis shows longitude. Gray dots correspond to sampling depths at the various stations.

and 270 m was two to three times higher in the Fe-fertilized patch than at the reference site (Table 1), which resulted in an excess of POC export of 1.5 to 2.5 mmol C m^{-2} day^{-1} in the fertilized waters. Comparing measurements of subsurface water column nitrate plus nitrite isotope ratios (δ^{15}N) [1.2 to 2.2 per mil (‰)] with the δ^{15}N of sinking PON (−0.5 ± 3.5‰ at 170 m and −0.2 ± 1.9‰ at 270 m, respectively), the N isotope budget (N_2 fixation end member = −1‰) revealed that N_2 fixation supported 77 to 84 ± 159% at 170 m and 64 to 75 ± 86% at 270 m of the export production in the Fe-fertilized area, consistent with the massive export of diazotrophs observed in the traps during the expedition (*3*, *29*). Collectively, these results suggest that the hydrothermally driven Fe fertilization fuels planktonic diazotrophs, which results in the low δ^{15}N of sinking PON and high POC export fluxes compared with subtropical systems not affected by hydrothermal activity (table S6) (*30*).

To confirm the causal link between hydrothermal inputs and diazotroph activity, we conducted experiments in which hydrothermally enriched waters collected at the Panamax site of volcano 1 (hereafter referred to as "plume water") were supplied to surface biological communities by using 300-liter reactors free of trace metals (fig. S7A and methods). Increasing volumes of plume water (from 0 to 14.5% of the total reactor volume) were added to surface seawater from outside of the direct volcanic

influence (21°40.98′S; 174°42.54′W). The plume water was characterized by low pH (6.4) compared with ambient seawater (8.1), and DFe concentrations (15.8 nmol liter^{-1}) were ~15-fold higher than those in ambient surface waters (1.0 nmol liter^{-1}) (table S7). The increasing additions resulted in consistent increases in DFe concentration and decreasing pH in the experimental reactors (fig. S7). Plume water additions enhanced N_2 fixation rates by a factor of seven to eight, on average, over all sampling days compared with those measured in the unamended control ($p < 0.05$, Mann-Whitney test) (Fig. 3A) and reached levels in the same range as in situ rates measured above the volcano (Fig. 2E). Likewise, as observed in situ, *Trichodesmium* abundances increased by a factor of three- to fivefold ($p < 0.05$, Mann-Whitney test) in plume water–amended reactors (Fig. 3B). Both N_2 fixation rates and *Trichodesmium* abundances decreased at the end of the experiment, likely as a consequence of phosphate depletion in the closed reactors (no possible turbulent diffusion) (fig. S7), but generally remained higher in the amended reactors compared with those measured in the control. Because of the low inorganic N:P molar ratio (~9:1) in the plume water (indicative of a greater phosphate availability relative to nitrate), the mixing of the plume water with surface seawater likely prevented the phosphate limitation for up to days 6 to 8, whereas nitrate was depleted after 2 days. This decoupling between nitrate and phosphate also mirrors the in situ data described above.

The Fe supply from the Tonga arc thus drives, in large part, the upper ocean phenology of biological activity. We estimate that the region of elevated Chla extends ~800 km in longitude and ~450 km in latitude (Fig. 2A), forming a hotspot of biological activity of ~360,000 km^2 in the middle of the otherwise desert-like WTSP. The trajectories of surface velocity program drifters deployed above volcano 1 indicate that over a 6-month period, Fe-fertilized water masses can be dispersed regionally and support this extended Chla patch (fig. S8). The trajectories provide a bulk representation of the complex dynamical processes occurring at smaller scales that involve the South Equatorial current modulated by mesoscale activity (*11*, *31*) or lateral stirring by filaments (*32*). In addition, multiple active vent fields have been (recently) identified along the Tonga arc and the Lau Basin (*16*, *17*, *33*, *34*), either at shallow depths (<500 m) or deeper (500 to 1000 m). Although all active shallow vents have not yet been discovered, with a density estimation of one active volcano center per 12 km of arc, fertilization processes such as those evidenced at volcano 1 likely occur at many locations along the arc, which further explains the regional extent of the Chla patch observed by satellite (Fig. 2A). We cannot exclude that the few emerged Tonga islands

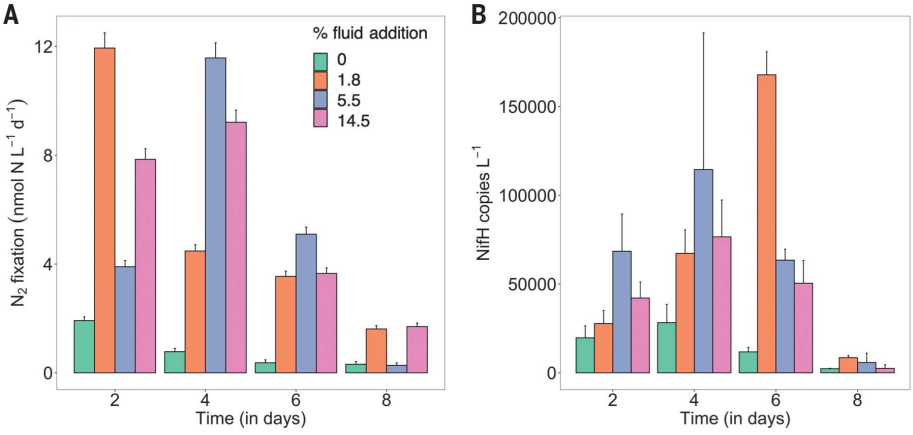

Fig. 3. Experimental evidence of the impact of hydrothermally enriched water additions on diazotroph communities. (**A** and **B**) Temporal evolution of (A) N_2 fixation rates (nmol N liter^{-1} day^{-1}) and (B) *Trichodesmium* abundances (*nifH* gene copies liter^{-1}) over the 196 hours of the experiment in the control treatment (no fluid addition) and in the reactors amended with 1.8, 5.5, and 14.5% of plume water collected at the Panamax site of volcano 1 (~200 m depth). Error bars correspond to standard deviations on triplicate analyses.

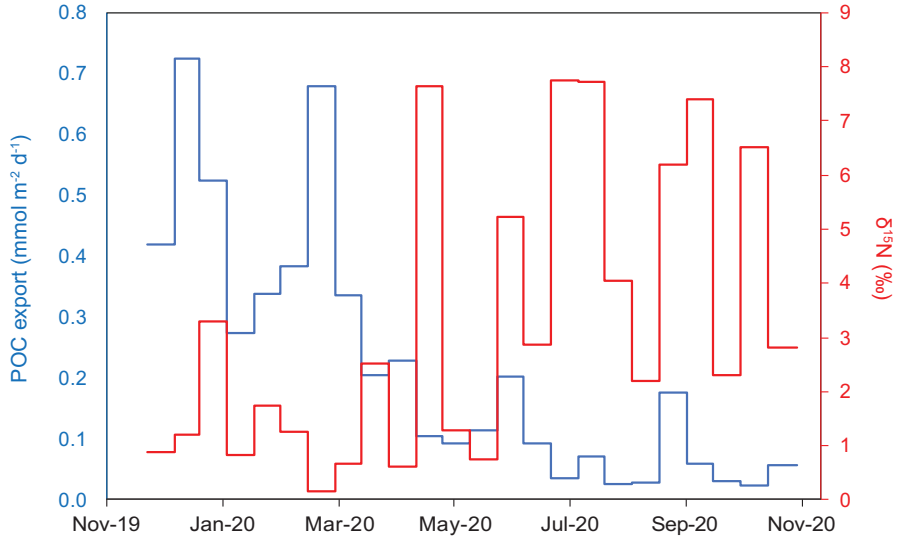

Fig. 4. Seasonal variability of export at 1000 m in the Fe-fertilized patch over 1 year. Fixed mooring deployed at 20°42.12′S; 177°51.96′W from November 2019 to November 2020 (see supplementary materials). The blue line represents POC export fluxes (mmol C m^{-2} day^{-1}), and the red line represents the $\delta^{15}N$ (‰) signature of exported PON.

could provide additional nutrients, likely contributing to the observed bloom. However, a study conducted over the entire tropical Pacific reveals that the mass effects of these islands are generally very localized (around the islands, with a Chla patch area of 9 to 13 km^2) and are of moderate amplitude (+9% of Chla increase relative to background waters) (*35*). By contrast, the bloom in the region of the Tonga volcanic arc is distinctive in that it is much larger (360,000 km^2) and of greater amplitude (~100% Chla increase) than around any other Pacific islands or archipelagos. This means that additional Fe sources of hydrothermal origin are necessary to sustain such a bloom. As an example, very weak Chla is observed around the Cook Islands, which are located at the same latitude as Tonga and receive the same amount of rainfall and aerosol Fe deposition annually but are not affected by hydrothermal activity (fig. S9), which confirms that nutrients of terrestrial origin are not sufficient to sustain blooms of large amplitude. Lastly, some extremely rare events such as the massive eruption of the Hunga Tonga Hunga Ha'apai volcano in January 2022 could also cause short-term localized blooms, such as the one observed by satellite after the eruption (*36*), that had no visible effect on the interannual trend of Chla. Other authors suggest that the interpretation

Table 1. Carbon and Fe budgets in the naturally fertilized region of the Tonga volcanic arc and the distal reference site, as well as comparisons with natural fertilizations in HNLC regions. Dashes indicate that these data are available but were not relevant to this study. n.a., not applicable.

Parameter	TONGA		CROZEX*†	KEOPS*‡
	+Fe (volcano 1)	−Fe (gyre)		
Bloom area (km^2)	360,000	No bloom	90,000	45,000
Bloom duration (days)	180	n.a.	58	75 to 105
Integrated Chla over the euphotic zone (mg Chla m^{-2})	39	n.a.	98.1	72 to 318
Vertical diffusivity (K_z) (m^2 s^{-1})	$3.7 \pm 1.9 \times 10^{-5}$	$5.2 \pm 9.6 \times 10^{-6}$	–	–
Vertical DFe gradient (mol m^{-4})	$3.1 \pm 4.7 \times 10^{-8}$	$7.8 \pm 3.1 \times 10^{-11}$	–	–
Vertical DFe diffusive flux (mmol Fe m^{-2} day^{-1})	$1.1 \pm 1.7 \times 10^{-4}$	$3.5 \pm 3.1 \times 10^{-8}$	6.0×10^{-5}	3.1×10^{-5}
Atmospheric DFe supply (mmol Fe m^{-2} day^{-1})§	2.0×10^{-5}	2.5×10^{-5}	1.0×10^{-4}	1.7×10^{-6}
Horizontal DFe supply (mmol Fe m^{-2} day^{-1})	0¶	0¶	3.9×10^{-4}	1.9×10^{-4}
Total DFe supply (mmol Fe m^{-2} day^{-1})	1.3×10^{-4}	2.5×10^{-5}	5.5×10^{-4}	2.2×10^{-4}
Total annual DFe supply (mmol Fe m^{-2})	4.7×10^{-2}	0.9×10^{-2}	20.0×10^{-2}	8.1×10^{-2}
POC export 170 m (mmol C m^{-2} day^{-1})	3.2	1.7	1.3**††	24.5**‡‡
POC export 270 m (mmol C m^{-2} day^{-1})	3.9	1.4		
"Excess" C sequestration efficiency 170 m (mol C mol^{-1} Fe)	13,600	n.a.	8640**	154,000**
"Excess" C sequestration efficiency 270 m (mol C mol^{-1} Fe)	23,000	n.a.		

*See Morris and Charrette (*59*). †See Pollard *et al*. (*39*). ‡See Blain *et al*. (*49*), updated by Chever *et al*. (*60*). §See Guieu *et al*. (*11*). ¶The main flux is from below; lateral advection is likely negligible. **Value for 200 m. ††Interpolated Th-derived POC export flux. ‡‡Th-derived POC export flux.

of the Chla increase after the eruption was distorted by the presence of abundant volcanic particles suspended in the water column after the eruption (*37*).

Looking more deeply into the 25-year monthly Chla time series (Fig. 2B and fig. S10), we find that, despite interannual variability, the bloom develops every year for at least 6 months in austral summer. This seasonal characteristic is probably linked to the thermal fitness of *Trichodesmium*, which are thought to only bloom at temperatures >25°C, reached in the WTSP between November and April (austral summer). This thermal constraint for *Trichodesmium* also probably explains why the bloom does not extend south of ~23°S, which marks the location of the 25°C isotherm. Further south, surface waters are also depleted in nitrate, and in the absence of diazotrophs, the newly emitted Fe supplied by hydrothermal vents along the arc cannot be taken up to produce new biomass. Because models predict a sea surface temperature increase of 1.5°C by the end of the century in the Tonga arc region (*38*), it is possible that the thermal constraint for diazotrophs will be relieved and the bloom will spread further south in the future.

To properly account for the seasonal variability of export, we deployed a moored sediment trap at 1000 m for a full annual cycle in the fertilized patch (see supplementary materials). We show that POC export was five times higher in austral summer than in winter (Fig. 4), resulting in a seasonally integrated (six summer months) POC export of 74 mmol C m^{-2}, that is, 80% of the annual POC export flux. The low $\delta^{15}N$ signature of sinking PON during these summer months (~0 to 1‰) confirms that N_2 fixation supports most export production during that season. In austral winter, the higher sinking PON $\delta^{15}N$ values (2 to 8‰) suggest that other N sources (i.e., deep nitrate) fuel the low export production. For comparison, the annual POC flux measured here in the subtropical ocean is of the same order of magnitude as that measured in the Southern Ocean in naturally Fe-fertilized waters (*39*, *40*). This suggests that Fe-fertilized regions of the oligotrophic ocean can act as net CO_2 sinks, provided sufficient phosphorus availability. The Fe-fertilized WTSP is a distinctive ecosystem that allows C sequestration supported by N_2 fixation owing to substantial winter phosphate replenishment (not associated with nitrate supply because of the decoupling of phosphacline and nitracline depths) (*25*) and to a turbulent diffusive flux of Fe and phosphate (19 mmol mol^{-1}) that meets *Trichodesmium* requirements (*41*). Furthermore, *Trichodesmium* can reduce its P quotas under P stress (*42*, *43*) and actively uses dissolved organic P compounds in this region (*44*), likely enhanced by high Fe availability (*45*). Taken together, these findings suggest that P and Fe work in concert to trigger extensive diazotroph blooms and C sequestration by N_2-based production in the WTSP.

Compared with shelf-driven natural Fe fertilizations that occur in HNLC (high nutrient, low chlorophyll) waters of the Southern Ocean, the TONGA bloom is generally more temporally and spatially extensive despite its lower intensity (depth-integrated Chla) (Table 1) (*39*, *46*–*48*). The total DFe flux in this study (130 nmol Fe m^{-2} day^{-1}) was generally lower than that measured in Fe-enriched waters downstream of the Kerguelen plateau [KEOPS cruise in 2005, 222 nmol Fe m^{-2} day^{-1} (*49*)] and downstream of the Crozet plateau [CROZEX cruise in 2004, 550 nmol Fe m^{-2} day^{-1} (*39*)] (Table 1). However, unlike HNLC regions, the surface waters of the WTSP are nitrate depleted, and only N_2-fixing organisms can exploit this newly emitted Fe to build biomass and drive carbon export to the deep ocean, as long as sufficient phosphorus remains available. Based on the excess POC export and the excess of DFe supply at the time of the cruise (Table 1), we calculated a C sequestration efficiency (defined as the ratio of the excess POC export to the amount of excess DFe supplied) of 13,600 and 23,000 mol C mol^{-1} Fe (at 170 and 270 m, respectively). Although comparisons between studies need to be considered with caution, given the different methods used and timescales considered, to estimate both excess Fe supply and POC export, this sequestration efficiency is higher than those from artificial mesoscale Fe-addition experiments [e.g., 4300 mol C mol^{-1} Fe for SOFeX (*50*) and 1200 mol C mol^{-1} Fe for SERIES (*51*)] and in the range of values measured in naturally fertilized HNLC regions [8600 mol C mol^{-1} Fe for CROZEX (*39*) to 154,000 mol C mol^{-1} Fe during KEOPS (*49*)]. This confirms that natural Fe fertilizations are more efficient for carbon sequestration than purposeful Fe additions. In addition, comparing such estimates from various natural oceanic settings, Le Moigne *et al*. (*52*) suggested that the apparent variability in C sequestration efficiency may be related to the timescale of Fe delivery (slow delivery being more efficient). Therefore, attention must be paid in future studies to the timescale of delivery of this

newly recognized mode of Fe supply through shallow hydrothermalism, including in temperate and polar ecosystems, where this efficiency could be even more important because of higher macronutrient availability.

Our conceptual view of the ocean Fe cycle has greatly evolved over the past 10 years and highlights the importance of hydrothermal activity on the Fe cycle (*53*). Although model simulations suggest that hydrothermal inputs associated with mid-ocean ridges (>2000 m) contribute 23% of the Fe found in the global ocean water column, that Fe only directly supports 3% of carbon export at 100 m (*54*). This is mostly because a large part of that Fe remains in the deep ocean over long timescales (*53*) and needs to be entrained in surface waters before potentially affecting photosynthetic communities (*46*, *48*). Fe from intermediate-depth (~1000 m) vents may also be transported long distances and, with the condition that these waters upwell, influence marine ecosystems located thousands of kilometers from the site of discharge (*55*). However, hydrothermal venting also occurs at shallower depths (<500 m) in island arc systems such as the Tonga arc. Even if scavenging and precipitation removes part of this newly emitted Fe from the dissolved pool (*23*), such shallow sources can rapidly supply Fe to overlying surface photosynthetic communities compared with Fe emitted at greater depths (*23*, *55*). In the oligotrophic ocean, the implications of such shallow hydrothermal Fe fertilization are highly important because they directly fuel surface diazotrophs and the export of organic matter to the deep ocean, representing regional hotspot sinks of atmospheric CO_2. We demonstrate here that shallow hydrothermal sources also represent a triggering factor on diazotroph blooms in regions where the atmospheric supply of DFe is virtually absent. Such forcing is of the utmost importance to study because climate models predict an expansion of the oligotrophic gyres (40% of our oceans) (*56*) where diazotrophs will likely thrive. Furthermore, in a warmer, more stratified ocean, such shallow Fe sources are likely to deliver Fe to surface communities more readily than deep sources (*55*). Beyond the oligotrophic oceans, shallow hydrothermal fertilizations are likely to be common in the global ocean because of the high number of shallow hydrothermal vents associated with island arc systems and submarine volcanic calderas (*57*), the exact numbers and locations of which are yet to be discovered (*14*). Such systems are also present at higher latitudes, notably in the HNLC waters in the subarctic Pacific and the Southern Ocean (*57*). Therefore, a comprehensive evaluation of their impact in these severely Fe-limited systems where surface mixed layers reach the intermediate or even the deep ocean water masses is clearly needed. Lastly, the extent to which such hydrothermal-driven biological carbon pump enhancement may have changed atmospheric CO_2 in the past remains unclear. Future studies would be relevant because the hydrothermal flux of Fe has been relatively constant over millennial timescales (*58*).

REFERENCES AND NOTES

1. C. M. Moore *et al*., *Nat. Geosci.* **6**, 701–710 (2013).
2. N. Gruber, in *Nitrogen in the Marine Environment* (Academic Press, 2008), pp. 1–50.
3. S. Bonnet *et al*., *ISME J.* **17**, 47–58 (2023).
4. D. M. Karl, M. J. Church, J. E. Dore, R. M. Letelier, C. Mahaffey, *Proc. Natl. Acad. Sci. U.S.A.* **109**, 1842–1849 (2012).
5. A. Subramaniam *et al*., *Proc. Natl. Acad. Sci. U.S.A.* **105**, 10460–10465 (2008).
6. J. P. Zehr, D. G. Capone, *Science* **368**, eaay9514 (2020).
7. C. Lory *et al*., *ISME Commun.* **2**, 41 (2022).
8. J. A. Sohm, E. A. Webb, D. G. Capone, *Nat. Rev. Microbiol.* **9**, 499–508 (2011).
9. S. Bonnet, M. Caffin, H. Berthelot, T. Moutin, *Proc. Natl. Acad. Sci. U.S.A.* **114**, E2800–E2801 (2017).
10. C. Schlosser *et al*., *Proc. Natl. Acad. Sci. U.S.A.* **111**, 1438–1442 (2014).
11. C. Guieu *et al*., *Sci. Rep.* **8**, 9075 (2018).
12. L. Bopp *et al*., *Biogeosciences* **19**, 4267–4285 (2022).
13. C. E. J. de Ronde, G. J. Massoth, E. T. Baker, J. E. Lupton, in *Volcanic, Geothermal, and Ore-Forming Fluids: Rulers and Witnesses of Processes Within the Earth*, vol. 10, S. F. Simmons, I. Graham, Eds. (Society of Economic Geologists, 2005), pp. 91–110.
14. C. R. German *et al*., *Philos. Trans. R. Soc. Londong Ser. A* **374**, 20160035 (2016).
15. J. E. Lupton, D. G. Pyle, W. J. Jenkins, R. Greene, L. Evans, *Geochem. Geophys. Geosyst.* **5**, Q01003 (2004).
16. P. Stoffers *et al*., *Geology* **34**, 453–456 (2006).
17. G. Massoth *et al*., *Geochem. Geophys. Geosyst.* **8**, Q11008 (2007).
18. C. Guieu, S. Bonnet, TONGA GEOTRACES GPpr14 ocean expedition. (2019), https://doi.org/10.17600/18000884.
19. C. Boulart *et al*., *Commun. Earth Environ.* **3**, 64 (2022).
20. W. W. Chadwick Jr. *et al*., *Geochem. Geophys. Geosyst.* **15**, 4325–4342 (2014).
21. N. Feuillet *et al*., *Nat. Geosci.* **14**, 787–795 (2021).
22. J. A. Resing *et al*., *Nature* **523**, 200–203 (2015).
23. C. Tilliette *et al*., *Global Biogeochem. Cycles* **36**, e2022GB007363 (2022).
24. J. Lavelle, I. Lozovatsky, D. Smith IV, *Geophys. Res. Lett.* **31**, L10308 (2004).
25. T. Moutin *et al*., *Biogeosciences* **15**, 2961–2989 (2018).
26. Y.-W. Luo *et al*., *Earth Syst. Sci. Data* **4**, 47–73 (2012).
27. A. Filella *et al*., *Front. Mar. Sci.* **9**, 923765 (2022).
28. F. Van Wambeke *et al*., *Biogeosciences* **15**, 2669–2689 (2018).
29. M. Benavides *et al*., *ISME J.* **16**, 2398–2405 (2022).
30. A. N. Knapp *et al*., *Biogeosciences* **15**, 2619–2628 (2018).
31. L. Rousselet *et al*., *Biogeosciences* **15**, 2411–2431 (2018).
32. A. de Verneil, L. Rousselet, A. M. Doglioli, A. A. Petrenko, T. Moutin, *Biogeosciences* **14**, 3471–3486 (2017).
33. S. E. Beaulieu, E. T. Baker, C. R. German, A. Maffei, *Geochem. Geophys. Geosyst.* **14**, 4892–4905 (2013).
34. C. R. German *et al*., *Philos. Trans. R. Soc. London Ser. A* **374**, 20160035 (2016).
35. M. Messié, A. Petrenko, A. M. Doglioli, E. Martinez, S. Alvain, *Nat. Geosci.* **15**, 469–474 (2022).
36. B. Barone, R. M. Letelier, K. H. Rubin, D. M. Karl, *Geophys. Res. Lett.* **49**, e2022GL099293 (2022).
37. A. Whiteside *et al*., *Front. Mar. Sci.* **9**, 1028022 (2023).
38. L. Dhage, M. J. Widlansky, *Earths Futur.* **10**, e2021EF002524 (2022).
39. R. T. Pollard *et al*., *Nature* **457**, 577–580 (2009).
40. M. Rembauville, I. Salter, N. Leblond, A. Gueneugues, S. Blain, *Biogeosciences* **12**, 3153–3170 (2015).
41. J. Nuester, S. Vogt, M. Newville, A. B. Kustka, B. S. Twining, *Front. Microbiol.* **3**, 150 (2012).
42. D. M. Karl, R. Letelier, D. V. Hebel, D. F. Bird, C. D. Winn, in *Marine Pelagic Cyanobacteria: Trichodesmiurn and Other Diazotrophs*, Nato Science Series C, E. J. Carpenter, D. G. Capone, J. G. Rueter, Eds. (Kluwer Academic Publishers, 1992), pp. 219–237.
43. A. E. White, Y. H. Spitz, D. M. Karl, R. M. Letelier, *Limnol. Oceanogr.* **51**, 1777–1790 (2006).
44. Z. Liang, R. T. Letscher, A. N. Knapp, *Nat. Geosci.* **15**, 651–657 (2022).
45. T. J. Browning *et al*., *Nat. Commun.* **8**, 15465 (2017).
46. M. Ardyna *et al*., *Nat. Commun.* **10**, 2451 (2019).
47. S. Blain, S. Bonnet, C. Guieu, *Biogeosciences* **5**, 269–280 (2008).
48. C. M. S. Schine *et al*., *Nat. Commun.* **12**, 1211 (2021).
49. S. Blain *et al*., *Nature* **446**, 1070–1074 (2007).
50. K. O. Buesseler, J. E. Andrews, S. M. Pike, M. A. Charette, *Science* **304**, 414–417 (2004).
51. P. W. Boyd *et al*., *Nature* **428**, 549–553 (2004).
52. F. A. C. Le Moigne *et al*., *Geophys. Res. Lett.* **41**, 4619–4627 (2014).
53. A. Tagliabue *et al*., *Nature* **543**, 51–59 (2017).
54. A. Tagliabue, O. Aumont, L. Bopp, *Geophys. Res. Lett.* **41**, 920–926 (2014).
55. W. Jenkins *et al*., *Earth Planet. Sci. Lett.* **539**, 116223 (2020).
56. J. J. Polovina, E. A. Howell, M. Abecassis, *Geophys. Res. Lett.* **35**, L03618 (2008).
57. J. A. Hawkes, D. P. Connelly, M. J. A. Rijkenberg, E. P. Achterberg, *Geophys. Res. Lett.* **41**, 942–947 (2014).
58. N.-C. Chu *et al*., *Earth Planet. Sci. Lett.* **245**, 202–217 (2006).
59. P. J. Morris, M. A. Charette, *Deep Sea Res. Part II Top. Stud. Oceanogr.* **90**, 147–157 (2013).
60. F. Chever, G. Sarthou, E. Bucciarelli, S. Blain, A. R. Bowie, *Biogeosciences* **7**, 455–468 (2010).

ACKNOWLEDGMENTS

The dataset presented here resulted from the efforts of many individuals both onboard and on land who contributed to the success of the expedition. We thank the captain and the crew of the reserach vessel *L'Atalante* (TGIR Flotte, operated by IFREMER), in particular, S. Laville Saint-Martin and J. Le Doare for their help during the multibeam survey, as well as the Technical Division INSU for technical support and equipment provision. We thank the captain and the crew of the research vessel *Alis* (TGIR Flotte, operated by IFREMER) for the safe recovery of the fixed mooring in particularly difficult weather conditions. We thank C. Dimier and the SAPIGH platform of the Institut de la Mer de Villefranche (IMEV) for sampling on board and performing the pigment analyses, and M. Tantillo for help with the noble gas extraction from water samples and isotope analysis performed at the noble gas laboratory of INGV-Palermo. We also thank H. Lucas Jr. for English editing. We thank J. P. Gattuso, S. Blain, A. Tagliabue, and L. Guidi for their advice on the manuscript. Lastly, we thank J. Resing and an anonymous reviewer for their constructive and valuable comments during the review process. **Funding:** This work was funded by Agence Nationale de Recherche grant ANR-18-CE01-0016 (S.B. and C.G.), A-MIDEX grant TONGA (S.B. and C.G., Excellence Initiative of Aix-Marseille University, a French "Investissements d'Avenir" program). Institut National des Sciences de l'Univers Les Enveloppes Fluides et l'Environnement grant TONGA (S.B. and C.G.), TGIR Flotte océanographique française TONGA cruise (C.G. and S.B.), the Institut de recherche pour le Développement (IRD) (S.B.), a MEMESTRA grant (C.B.), and National Science Foundation grant NSF-OCE 1829797 (A.N.K.). Finally, this project has received funding from the European FEDER Fund under project 1166-39417. **Author contributions:** Conceptualization: S.B., C.G.; Methodology: S.B., C.G., C.B., F.G.; Investigation: S.B., C.G., V.T., C.B., F.G., M.B., D.G.-S., J.-M.G., O.G., J.H., C.L., E.P.-V., G.S., C.T.; Data curation: S.B., C.G., V.T., C.B., P.B.-A., C.S., F.G., M.B., A.N.K., Y.C., D.G.-S., H.J.F., J.H., N.L., S.N., A.L.R., G.S., C.T., A.L.-D., F.A.C.L.M., M.J.-C.; Visualization: S.B., C.G., C.B., F.G., P.B.-A., A.N.K., and H.J.F., A.L.-D., F.A.C.L.M., M.J.-C.; Writing – original draft: S.B., C.G.; Writing – review and editing: All authors. **Competing interests:** The authors declare that they have no competing interests. **Data and materials availability:** All data are available in the main text or the supplementary materials. The $\delta^{15}N$ data are deposited in the BCO-DMO database (https://www.bco-dmo.org/dataset/869963), the data are deposited in the SEANOE database (https://campagnes.flotteoceanographique.fr/campagnes/18000884/). **License information:** Copyright © 2023 the authors, some rights reserved; exclusive licensee American Association for the Advancement of Science. No claim to original US government works. https://www.science.org/about/science-licenses-journal-article-reuse

SUPPLEMENTARY MATERIALS

science.org/doi/10.1126/science.abq4654
Materials and Methods
Figs. S1 to S10
Tables S1 to S8
References (*61*–*96*)

Submitted 12 April 2022; accepted 21 April 2023
10.1126/science.abq4654